OPEN ACCESS

Materials Chemistry REPORT

The Innovation Materials

Functionalized flash graphene membrane with turbostratic stacking enables ultrafast water purification

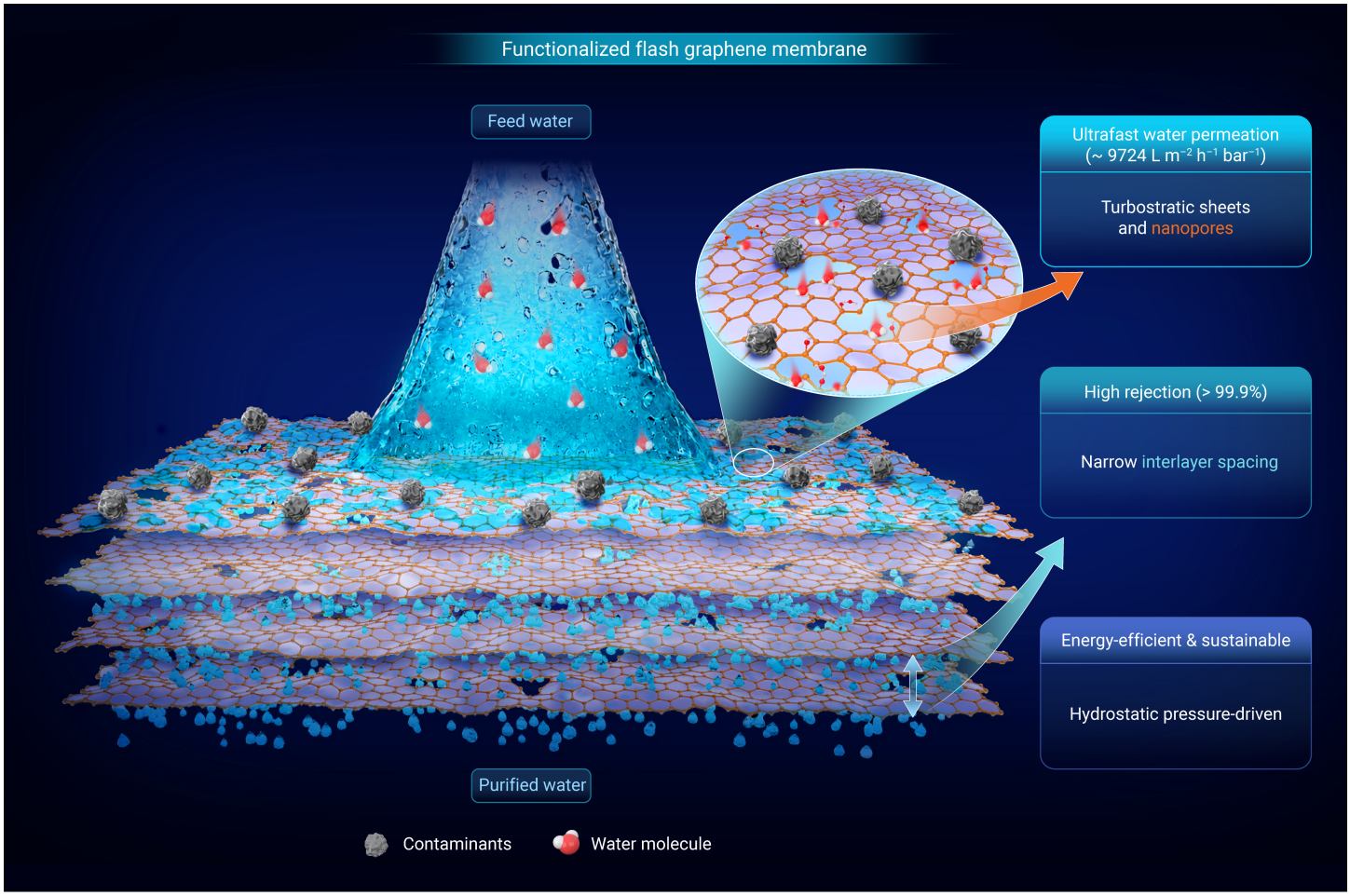
Chao Jia,[1,2,14] Junjie Chen,[3,14] Xing Liu,[3,14] Yong Liu,[4,14] Linghui Yan,[3] Jiewen Luo,[5] Ruizhe Xu,[6] Xiaohu Zhang,[3] Shicheng Zhang,[2] Yong Jiang,[7] Beibei Xiao,[8] Jinsong Wu,[9] Shihong Lin,[10] Jiabao Zhang,[1] Minghong Wu,[11,*] Yujun Wang,[1,12,*] Guosheng Shi,[3,*] Xiangdong Zhu,[1,2,*] and Fengchang Wu[5,13,*]

*Correspondence: mhwu@fzu.edu.cn (M.W.); yjwang@issas.ac.cn (Y.W.); gsshi@shu.edu.cn (G.S.); zxdjewett@fudan.edu.cn, xdzhu@issas.ac.cn (X.Z.); wufengchang@vip.skleg.cn (F.W.)

Received: June 11, 2026; Accepted: September 10, 2026; Published Online: September 10, 2026; https://doi.org/10.59717/j.xinn-mater.2026.100244

© 2026 The Author(s). This is an open access article under the CC BY license (https://creativecommons.org/licenses/by/4.0/).

GRAPHICAL ABSTRACT



PUBLIC SUMMARY

- Functionalized flash graphene membrane with turbostratic sheets and nanopores enables fast water transport.
- Narrow interlayer spacing of the membrane ensures the efficient rejection (> 99.9%) of various contaminants.
- Scalable, energy-efficient fabrication suitable for household and on-site water purification.

REPORT Materials Chemistry

OPEN ACCESS

www.the-innovation.org/the-innovation-materials

Functionalized flash graphene membrane with turbostratic stacking enables ultrafast water purification

Chao Jia,[1,2,14] Junjie Chen,[3,14] Xing Liu,[3,14] Yong Liu,[4,14] Linghui Yan,[3] Jiewen Luo,[5] Ruizhe Xu,[6] Xiaohu Zhang,[3] Shicheng Zhang,[2] Yong Jiang,[7] Beibei Xiao,[8] Jinsong Wu,[9] Shihong Lin,[10] Jiabao Zhang,[1] Minghong Wu,[11,*] Yujun Wang,[1,12,*] Guosheng Shi,[3,*] Xiangdong Zhu,[1,2,*] and Fengchang Wu[5,13,*]

[1]State Key Laboratory of Soil and Sustainable Agriculture, Institute of Soil Science, Chinese Academy of Sciences, Nanjing 210018, China

[2]Department of Environmental Science and Engineering, Fudan University, Shanghai 200433, China

[3]Shanghai Key Laboratory of Atomic Control and Application of Inorganic 2D Supermaterials, State Key Laboratory of Materials for Advanced Nuclear Energy, Shanghai Applied Radiation Institute, Shanghai University, Shanghai 200444, China

[4]International School of Materials Science and Engineering, State Key Laboratory of Advanced Technology for Materials Synthesis and Processing, Wuhan University of Technology, Wuhan 430070, China

[5]Guangdong Key Laboratory of Integrated Agro-environmental Pollution Control and Management, Institute of Eco-environmental and Soil Sciences, Guangdong Academy of Sciences, Guangzhou 510650, China

[6]Maseeh Department of Civil, Architectural, and Environmental Engineering, The University of Texas at Austin, Austin, Texas 78712, United States

[7]Fujian Provincial Key Laboratory of Soil Environmental Health & Regulation, College of Resources & Environment, Fujian Agriculture & Forestry University, Fuzhou 350002,China

[8]School of Energy and Power Engineering, Jiangsu University of Science and Technology, Zhenjiang 212003, China

[9]Nanostructure Research Center, Wuhan University of Technology, Wuhan 430070, China

[10]Department of Civil and Environmental Engineering and Chemical and Biomolecular Engineering, Vanderbilt University, Nashville 37235-1831, United States

[11]School of Future Technology, Fuzhou University, Fuzhou 350000, China. Key Laboratory of Organic Compound Pollution Control Engineering (MOE), School of Environmental and Chemical Engineering, Shanghai University, Shanghai 200444, China

[12]University of Chinese Academy of Sciences, Nanjing 211135, China

[13]State Key Laboratory of Environmental Criteria and Risk Assessment, Chinese Research Academy of Environmental Sciences, Beijing 100012, China

[14]These authors contributed equally

*Correspondence: mhwu@fzu.edu.cn (M.W.); yjwang@issas.ac.cn (Y.W.); gsshi@shu.edu.cn (G.S.); zxdjewett@fudan.edu.cn, xdzhu@issas.ac.cn (X.Z.); wufengchang@vip.skleg.cn (F.W.)

Received: June 11, 2026; Accepted: September 10, 2026; Published Online: September 10, 2026; https://doi.org/10.59717/j.xinn-mater.2026.100244

© 2026 The Author(s). This is an open access article under the CC BY license (https://creativecommons.org/licenses/by/4.0/).

Citation: Jia C., Chen J., Liu X., et al. (2026). Functionalized flash graphene membrane with turbostratic stacking enables ultrafast water purification. *The Innovation Materials* **4**:100244.

Currently, the potentially high permeability of graphene oxide (GO) membranes is fundamentally limited by their long and tortuous diffusion channels (*Z*-channels). To address this dilemma, we introduced a continuous flash Joule heating method to synthesize functionalized flash graphene (FFG) membranes with turbostratically stacked sheets that formed interconnected water transport channels. Meanwhile, the combination of misaligned nanopores within the sheets and the narrow interlayer spacing generated numerous thin *S*-channels, which also accelerated water transport. Thus, the FFG membrane can easily achieve a water permeance (~ 9724 L m^{-2} h^{-1} bar^{-1}) that was two orders of magnitude higher than that of conventional GO membranes. The trajectories of water molecules were tracked by molecular dynamics, confirming that the formed misaligned nanopores significantly shorten the transport distance of water molecules. Importantly, this membrane exhibited efficient rejection (> 99.9%) of various heavy metal ions, organic molecules, and nano-plastics due to its narrow interlayer spacing. Overall, this work facilitates the scalability and economy of FFG membrane fabrication, expanding the demand for on-site and household water purification in the entire membrane field.

INTRODUCTION

Suitably engineered graphene-based membranes effectively tackle diverse water dilemmas, owing to their exceptional properties that enable rapid water transport while achieving selective sieving of ions and molecules.[1-8] Compared to conventional polymeric and ceramic membranes with broad pore size distributions and limited tunability, graphene-based membranes offer atomic-level precision in tailoring pore size and interlayer spacing, enabling highly efficient separations.[9-11] It has been established that water penetration can be easily achieved by creating uniform sub-nanometer pores in graphene monolayers or by constructing two-dimensional channels between graphene oxide (GO) nanosheets.[12,13] However, the former approach necessitates the construction of isoporous membranes with pore diameters of <0.55 nm over lateral dimensions exceeding the micrometer level to achieve excellent selectivity in actual separation processes.[14-16] Notably, conventional strategies for fabricating these structures (such as chemical etching) suffer from harsh, time-consuming processes while simultaneously struggling to control the spatial stacking behavior of the etched nanosheets.[13,17] In the latter approach, water molecules travel through a *Z*-channel across the narrow interlayer spacing, leading to an extended transport distance, which directly results in low permeability.[18-20] Moreover, methods that increase the interlayer spacing, such as intercalation, lead to a critical challenging trade-off between permeability and selectivity.[21,22]

A promising strategy is to combine the above two approaches to fabricate highly efficient graphene membranes that ideally possess suitable pore sizes to maximize permeability while maintaining narrow interlayer spacing for excellent selectivity. For water molecules, they will not only pass through these nanopores of each layer, but also permeate through the interlayer spacing. Notably, pore channels provide faster transport pathways due to the reduced friction compared to the confined interlayer spacing.[23,24] As a result, the actual path-length of water molecules (thin *S*-channel) is less tortuous than that of stacked GO membranes (*Z*-channel), which undoubtedly shortens their transport distance and enables the membrane to achieve high water permeance. In theory, larger pores in the membranes are more advantageous for the transport of water molecules within the two-dimensional nanochannels.[25,26] Intuitively, however, infinitely increasing the pore size may lead to the vertical alignment of the pores existing between the upper and lower layers of the graphene-based membrane. Potentially, solutes will escape directly from these through-pores (*I*-channel) without being rejected by the interlayer spacing, which will greatly compromise the selectivity of the membrane. Therefore, constructing effective steric hindrance by regulating appropriate pore remains a key challenge for designing efficient graphene membranes. Although many current in-pore-formation approaches can regulate the size of nanopores through the microenvironment there is no method that can simultaneously promote the formation of graphene structure and pore structure in-situ on the carbon-containing substrate, which is essential for the large-scale preparation of porous graphene.

Herein, a loosely stacked functionalized flash graphene (FFG) membrane with turbostratically arranged sheets was elaborately constructed with the aid of flash Joule heating (FJH) technology, forming interconnected water transport channels. Meanwhile, the misaligned nanopores within the sheets and

the interlayer spacing jointly formed numerous thin *S*-channels, effectively shortening the water transport pathways, thereby achieving significantly enhanced water permeance (~ 9724 L m^{-2} h^{-1} bar^{-1}) while maintaining high selectivity (>99.9%). This study broadens the possibilities for synthesizing and applying advanced functional membranes, contributing to sustainable development strategies.

MATERIALS AND METHODS

FJH-induced synthesis of FG with porous structure

Flash graphene (FG) was laboratory-prepared by a flash Joule heating (FJH) technique involving ultra-high temperature graphitization (> 3000 K) and electric field exfoliation.[27,28] To prepare FG with a porous structure, 0.2 g of the obtained porous carbon material was put into a quartz tube (tube thickness: 2 mm, inner diameter: 6 mm, length: 45 mm) of laboratory scale devices and compressed with copper electrodes to obtain a low resistivity (< 2 Ω). Then, the loaded quartz tube was placed in a vacuum desiccator (~0.6 psi) and operated on the continuous alternating current FJH (AC-FJH) and direct current FJH (DC-FJH) processes at the desired condition.[28] To investigate the effect of FJH parameters on the pore size structure and graphitization of the obtained FG materials, different reaction voltages and times were set. The voltages of the AC-FJH process were set to 100 V and 150 V, respectively, with discharge time being 6 s. The voltages of the DC-FJH process were set to 100 V and 150 V, and the discharge times were 10 ms and 30 ms, respectively.

To continuously produce FG materials on a large scale, we also employed integrated automation equipment to assist.[29] Due to differences in electrode diameters between the laboratory scale device (6 mm) and the integrated automated equipment (8 mm), the contact cross-sectional area of the sample increases, leading to a decrease in current density during the FJH reaction. Therefore, to ensure that the sample receives the same amount of Joule heating during continuous production, it is necessary to readjust the discharge voltage of the integrated automated equipment or modify the sample loading weight to compensate for the amplification effects between the two devices. Detailly, 0.2 g of porous carbon material was put into a quartz tube (tube thickness: 3 mm, inner diameter: 10 mm, length: 40 mm) and then placed vertically on the sample tray. After startup, the equipment began to run fully automatically. Subsequently, the robot arms gradually grabbed the loaded quartz tube from the sample tray to the reaction zone and blanking zone, ending a cycle of the FJH reaction. The discharge parameters of the AC-FJH process were set to 120 V, 6 s and those of the DC-FJH process were set to 200 V, 30 ms.

Preparation of FFG membranes

The as-prepared FG substrate, initially as a powder, required an oxidation treatment of approximately 48 h to form a functionalized membrane material. This treatment introduced hydrophilic groups, such as hydroxyl and carboxyl groups, which improved the aqueous dispersibility of the highly crystalline and intrinsically hydrophobic FG and promoted interlayer hydrogen bonding during membrane assembly, thereby facilitating the formation of the FFG membrane. First, 0.5 g of powdered FG was placed in a solution mixed with sulfuric acid (8 mL), potassium persulfate (1 g) and phosphorus pentoxide (1 g), and stirred at a constant temperature of 353 K for 4.5 h. Then, 300 mL of DI water was added to the above solution and allowed to stand for about 12 h. After filtration, the solid product was dried at 353 K for 6 h. Further, the crushed solid product was dissolved in sulfuric acid (40 mL), then potassium permanganate (4 g) was slowly added, and the mixed solution was continued to stir for 2 h. The temperature should stabilize below 283 K in an ice bath. In addition, 50 mL of DI water was slowly added to the solution and continued stirring for 2 h. During this process, the temperature was controlled below 293 K using an ice bath. After stirring, 300 mL of DI water was added to the solution, and hydrogen peroxide (20 mL) was immediately added for further oxidation, followed by stirring the solution for 12 h. After filtration, the solid product was washed twice with hydrochloric acid (2 mol L^{-1}) and DI water to remove impurities. Subsequently, the collected sample was diluted to 200 mL with DI water, and the concentration of the FFG was approximately 2.5 mg mL^{-1}. Finally, the FFG membrane was prepared on the cellulose acetate membrane substrates by simple vacuum filtration using the obtained FFG suspension.

Performance test of FFG membranes

The separation performance of FFG membranes was typically evaluated by filtering different types of ions or molecules, including metal ions, dye molecules, and microplastic nanoparticles. The initial concentrations of metal salts and dyes were 50 mg L^{-1} and 10 mg L^{-1}, respectively, while that of microplastics was 1 mg L^{-1}. These relevant tests were all conducted on a homemade dead-end filtration device at room temperature. The effective membrane area for separation was approximately 2 cm^2. We also prepared a large area of FFG membrane was expected to be applied to the actual scenario of water purification. At the same time, metal ions (5 mg L^{-1} $FeCl_3$) and emerging persistent organic pollutants (10 μg L^{-1} PFOA) were used as probes to investigate the separation performance of the FFG membrane.

Molecular dynamics (MD) simulations

To verify the feasibility of the nanofiltration performance of FFG membrane with *S*-channels, molecular dynamics (MD) simulations were performed to compare two filtration systems of perfect and defective graphene sheets, respectively. All MD simulations were performed in the NVT ensemble using the NAMD 2.14 version with a time step of 1.0 fs.[30] The V-rescale temperature coupling was applied every 20 steps to keep the system at 300 K. The parameters of graphene were referred to as previous research,[31-33] and the rigid TIP3P water model was used for water molecules.[34] Periodic boundary conditions were used in all three directions. All parameters were from the CHARMM force field.[35] The particle-mesh Ewald method with a real space cutoff of 12 Å was used to treat long-range electrostatic interactions and the same cutoff was applied to the van der Waals interactions.[36] Periodic boundary conditions were applied to all three coordinates.

RESULTS AND DISCUSSION

Thin *S*-channel abundance by nanopores for an ultrafast FFG membrane

In theory, the designed graphene membrane should exhibit a narrow interlayer spacing to achieve excellent selectivity and an appropriate pore size to maximize permeability. Based on this, a "two-wheel drive" strategy was adopted to instantly convert biomass-derived porous carbon (PC) materials into FG in situ while inheriting the associated nanopores via FJH technology (Figure 1A & Table S1). After undergoing ultra-high temperature graphitization (> 3000 K) and electric field exfoliation in a bottom-up FJH strategy,[27,28] PC-1 sample-derived FG with an average stacking number of about 6 layers was obtained, as confirmed by Raman, X-ray diffraction (XRD), atomic force microscopy (AFM), scanning transmission electron microscope (STEM), and high-resolution transmission electron microscopy (HR-TEM) results (Figures 1B–E & S1–S7). Furthermore, the pore structure (< 3 nm) was inherited from the parent PC-1 sample to the maximum extent (Figures 1D-F, & S8). And typical PC-1 sample-derived FG had the 1292 m^2 g^{-1} of BET surface areas suggested much defective structures, which can be confirmed by the high sp^3/sp^2 ratio (26.4%) in the X-ray photoelectron spectroscopy (XPS) spectrum (Figures S2 & S9). This result indicated that the derived membrane material enabled the formation of numerous *S*-channels, facilitating faster water transport and achieving well-defined selectivity.

After oxidation treatment of the PC-1 sample-derived FG, the nanopore size of its derived functionalized flash graphene (FFG) was mainly concentrated around 3.5 nm (Figure 1G). The PC-1 sample-derived FFG nanosheets exhibited an average thickness of 1.5 nm, with lateral dimensions primarily ranging from 0.5 to 2.0 μm, consistent with previous studies (Figures S10–S11).[37,38] Further, the PC-1 sample-derived FFG membrane was fabricated by a vacuum filtration method (Figure S12). Notably, the above oxidation process introduced functional groups such as hydroxyl, carboxyl, and epoxy onto the FFG membrane,[39,40] which unsurprisingly further increased the defect degree (Figures S13–S15). As shown in Figure S16, the surface of this FFG membrane exhibited mostly uneven planes, with many distinguishable wrinkles evenly distributed.[41] Moreover, the PC-1 sample-derived FFG membrane (approximately 120 μm in thickness) exhibited a loosely stacked architecture consisting of misoriented graphene nanosheets and inherent porosity (Figure 1H). Meanwhile, the cross-sectional images of this FFG membrane revealed a distinct two-dimensional lamellar structure, which was

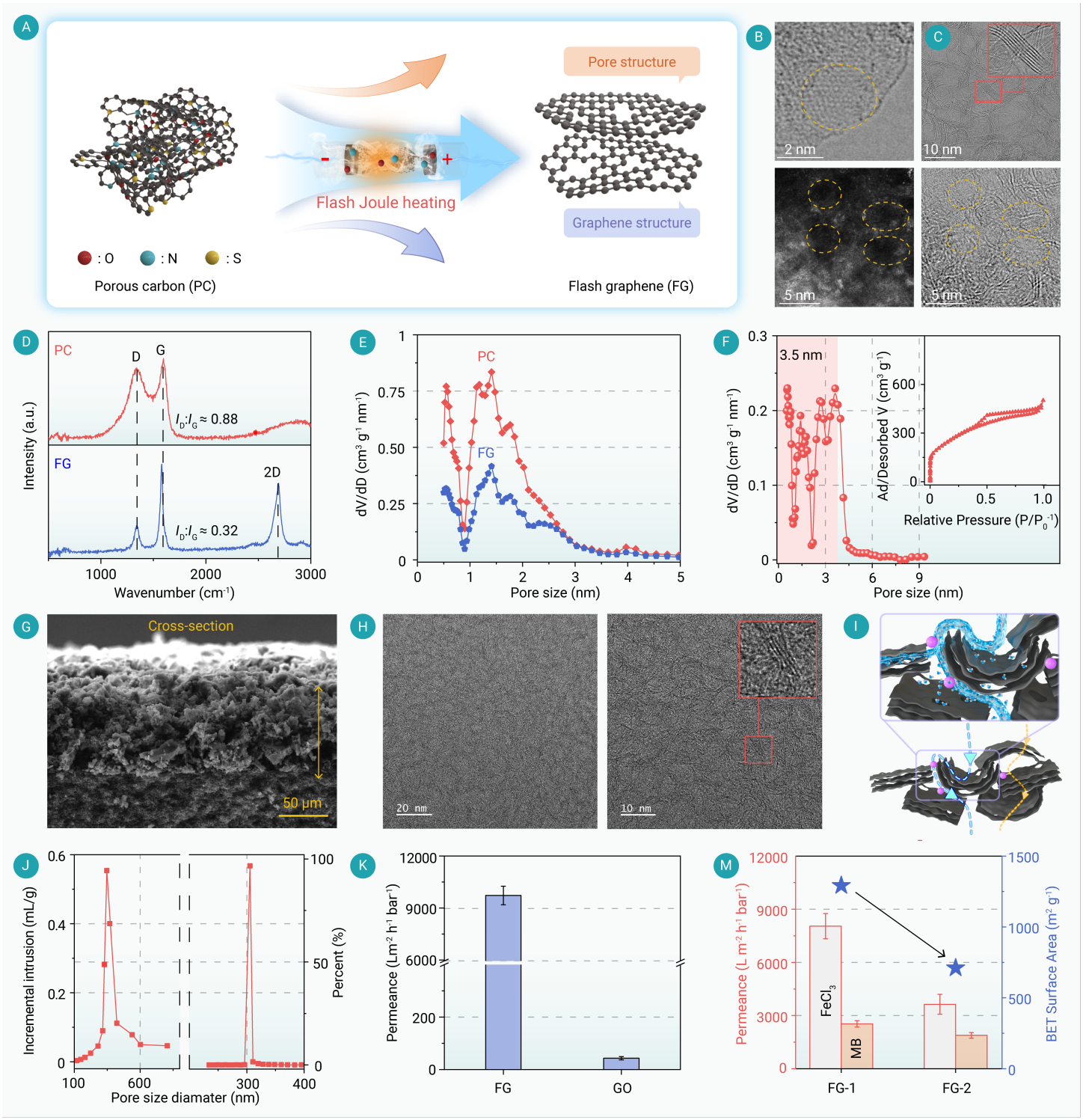


Figure 1. Thin *S*-channels constructed from nanopores in a functionalized flash graphene (FFG) membrane (A) Schematic of the flash Joule heating (FJH)-assisted synthesis process of flash graphene (FG). Porous carbon (PC) was rapidly heated in the reactor for conversion into FG. (B) and (C) High-resolution transmission electron microscopy (HR-TEM) images of PC-1 sample-derived FG. (D) Scanning transmission electron microscopy (STEM) image of PC-1 sample-derived FG. (E) Raman spectra of PC-1 sample and its derived FG. The FG had a low-intensity D peak, indicating the absence of considerable defects. The intensity ratio (~ 0.79) of the 2D and G bands demonstrated that the FG consisted mainly of few-layered graphene structures. (F) Pore size distributions of the PC-1 sample and its derived FG. (G) Pore size distribution (inset: N_2 adsorption-desorption isotherms) of the PC-1 sample-derived FFG. After oxidation FJH treatment, the BET surface area of FFG-2 was 1181 m^2 g^{-1}. (H) Cross-sectional scanning electron microscope (SEM) images of the PC-1 sample-derived FFG membrane. (I) Cross-sectional TEM images of the PC-1 sample-derived FFG membrane. (J) The structural diagram of the FFG membrane. (K) The pore size of PC-1 sample-derived FFG membrane obtained through mercury intrusion porosimetry (left) and capillary flow porometer (right) methods, respectively. (L) Comparison of water permeance of the as-synthesized graphene oxide (GO) membrane and PC-1 sample-derived FFG membranes under 1 bar. (M) Relationship between the BET surface areas of FG samples and the separation performance of their derived membranes (10 mg L^{-1} methylene blue and 50 mg L^{-1} $FeCl_3$ aqueous solutions at 1 bar). The precursors for the synthesis of these membranes were FGs with different pore structures, as detailed in Table S2.

consistent with the in-situ cross-sectional images obtained via focused ion beam (FIB) milling, thereby contributing to the enhanced selectivity of the FFG membrane (Figures 1I, S17-S18). This unique morphological arrangement created voids between adjacent nanosheets, forming interconnected channels that promoted high water permeability (Figures 1J–K).

The PC-1 sample-derived FFG membrane also exhibited excellent

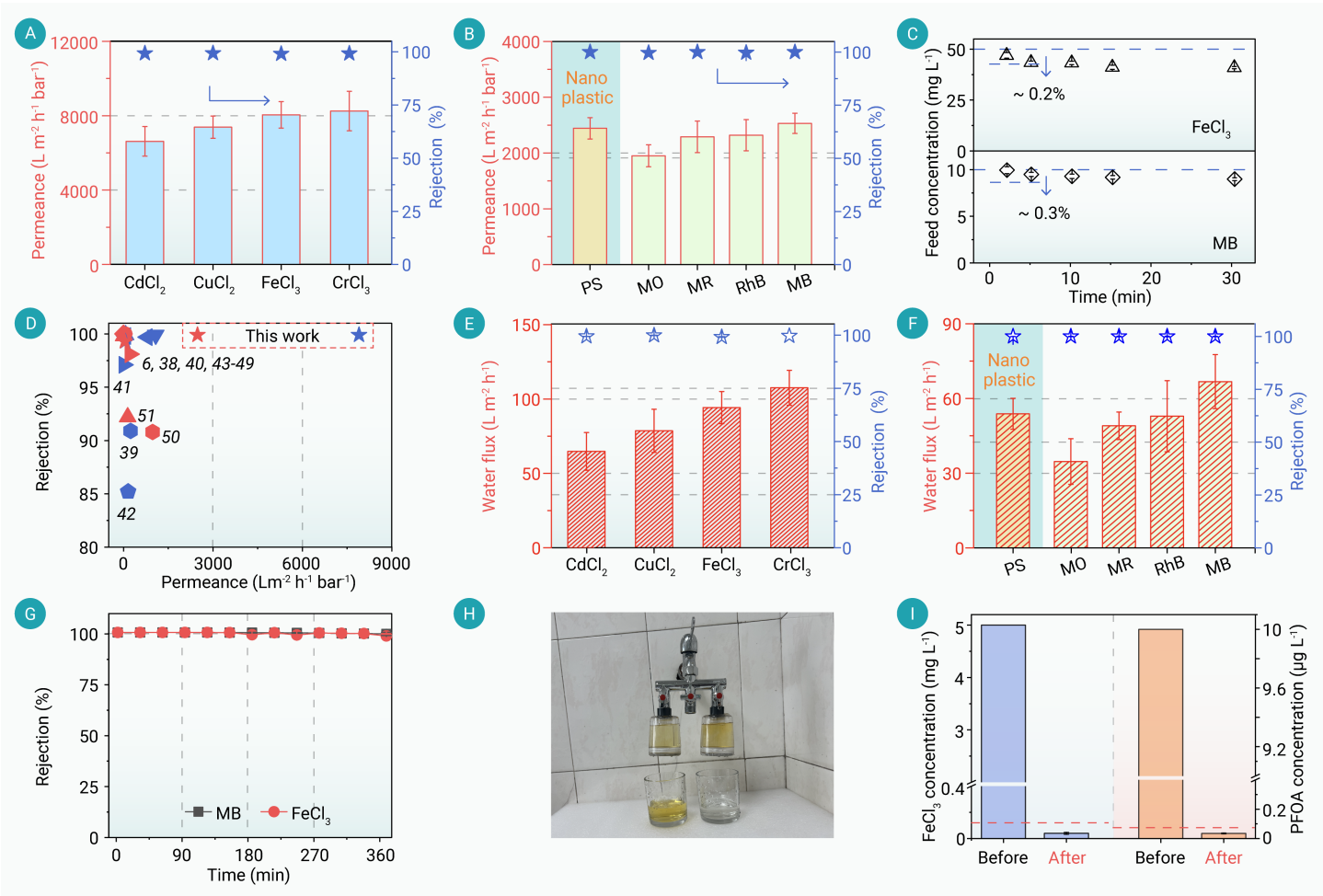


Figure 2. Separation performance of PC-1 sample-derived FFG membranes (A) FFG membrane for the separation of four different metal chloride aqueous solutions with a constant concentration of 50 mg L^{-1} at 1 bar. (B) FFG membrane for the separation of nano-plastic (polystyrene microspheres, PS) and four different dye aqueous solutions with a constant concentration of 10 mg L^{-1} at 1 bar. (C) Concentration variations of $FeCl_3$ and MB solutions adsorbed by the FFG membrane as a function of adsorption time. Error bars indicated the standard deviation from three different samples. (D) Comparison of Fe^{3+} (blue) and MB (red) rejection and water permeance between FFG membrane in this work and other state-of-the-art membranes (see more information in Supplementary Table 4). (E) FFG membrane for separation of four different metal chloride aqueous solutions (50 mg L^{-1}) without additional operating pressure. (F) FFG membrane for separation of PS and four different dye aqueous solutions (10 mg L^{-1}) without additional operating pressure. (G) MB and $FeCl_3$ rejection stability of the FFG membrane during continuous filtering operation for 360 min without additional operating pressure (10 mg L^{-1} MB and 50 mg L^{-1} $FeCl_3$ aqueous solutions). (H) Photo of the filter cup with a blank membrane (left) or FFG membrane (right) for purifying household drinking water. (I) Separation performance of the as-synthesized FFG membrane for actual wastewater containing $FeCl_3$ and perfluorooctanoic acid (PFOA) (5 mg L^{-1} $FeCl_3$ and 10 μg L^{-1} PFOA aqueous solutions).

hydrophilicity (Figure S19). Compared with the dry state (8.37 Å), the interlayer spacing of this FFG membrane in pure water and different salt solutions gradually increased within the range of 10.0 Å to 12.1 Å (Figure S20), indicating unavoidable swelling similar to conventional GO membranes. In contrast to traditional GO membranes, water molecules were transported solely through *Z*-channels.[2] The FFG membrane consisted of loosely assembled turbostratic graphene sheets, with inter-sheet voids and interconnected channels. Meanwhile, the combination of misaligned nanopores within the sheets and the narrow interlayer spacing generated numerous thin S-channels (Figure 1J). Consequently, the FFG membranes transported water molecules through numerous thin *S*-channels and interconnected channels, significantly shortening the path-length of water molecules. As shown in Figure 1L, the water permeance of the PC-1 sample-derived FFG membrane was approximately 160 times higher than that of the traditional GO membrane, reaching 9724 L m^{-2} h^{-1} bar^{-1}.

Notably, changes in the pore structure and graphitization degree of the parent porous carbon materials during FJH treatment were dynamic processes that were influenced mainly by the FJH parameters and their properties. Generally, increasing energy input in the FJH system favored the rearrangement of carbon atoms in the parent carbon materials to form FG while simultaneously accelerating the collapse of the nanopore structure.[28] As shown in Figures S21–S29, this regulation reduced the BET surface area of the obtained FGs. Based on these results, the continuous AC-FJH condition was set to 100 V for 6 s, and the DC-FJH condition to 150 V for 30 ms. Furthermore, the parent carbon materials with high sulfur content and BET surface area were more likely to maintain a relatively high porosity during the FJH reaction (Figures S30–S33 & Table S1). In summary, the FG with high BET surface area and well-developed micropores was selected, which facilitated the construction of thin *S*-channels in the membrane, thereby significantly enhancing water permeance (Figures 1M, S34 & Table S2).

Evaluation of separation performance of FFG membranes

To explore separation performance of FFG membranes (with FG-1 sample as precursor, Table S2), various pollutants were chosen as probes, ranging from ions to nano-particles, including heavy metal chlorides ($FeCl_3$, $CuCl_2$, $CrCl_2$, and $CdCl_2$), organic dyes (methyl blue, methyl orange, methyl red, and rhodamine B), and nano-plastics (polystyrene). The structures and sizes of these pollutants were listed in the Table S3. As illustrated in Figures 2A-B & S35-S36, the FFG membrane exhibited excellent and stable separation efficiency (> 99.9%) for these pollutants. The limited oxygen functional groups and unique water transport channels of the FFG membrane reduced the contact between pollutants and the membrane, resulting in minimal adsorption. This was confirmed by the adsorption process in Figure 2C, which showed a mere 0.3% of the pollutants were retained via adsorption. Consequently, the separation performance of the FFG membrane did not originate from a thin, highly ordered layered structure similar to that of GO membranes,

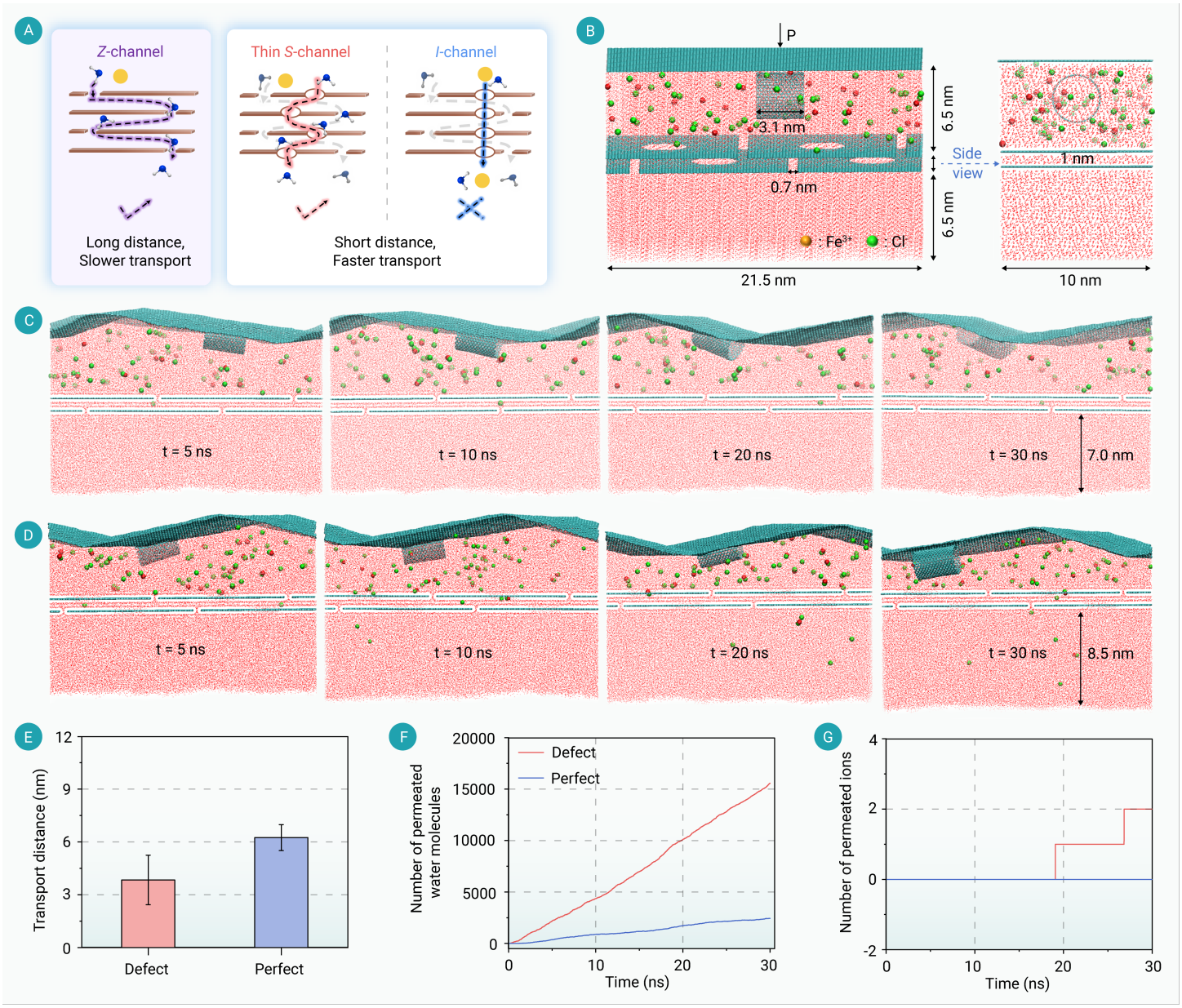


Figure 3. Theoretical guidance for the synthesis of FFG membranes with S-channels (A) Schematic illustration showed the key strategy used in this work. The interlayer spacing of graphene allowed the permeation of water molecules (H, white; O, blue) but excluded pollutants (yellow spheres). The misaligned nanopores permitted both water molecules and pollutants to penetrate. For traditional GO membranes, water molecules followed only a *Z*-channel (purple) to cross the interlayer spacing, resulting in long distances and slow transport. For the designed FFG membrane, water molecules were transported through nanopore channels, including misaligned pores (thin *S*-channel, red) and through-pores (*I*-channel, blue), which shortened the distance and enabled faster transport. Notably, solutes escaped directly from the *I*-channel without being rejected by the interlayer spacing. (B) The structure and size of the sheets on the designed FFG membranes with misaligned nanopores (defect system) and without nanopores (perfect system). Top and side views of water molecules and ions passed through the defect system in a molecular dynamics (MD) simulation. The snapshots of the water, ions, and particles passed through nanochannels in (C) perfect and (D) defect systems, respectively. (E) Comparison of the average transport distance of water molecules that permeated through each graphene layer in defect and perfect systems. (F) The number of water molecules that passed through the perfect system and the defect system changes with time. The number of water molecules at time (t) is defined as the difference between the total number of water molecules passing through the membrane from the feed side to the draw side and the opposite direction. (G) The number of Fe^{3+} that passed through the perfect system and the defect system changed with time.

but rather from interlayer channels that run throughout the membrane, collectively providing effective steric hindrance.[42]

In addition, benefiting from the distinctive *S*-channels, the FFG membrane simultaneously achieved enhanced water permeance and efficient removal of pollutants (such as nano-plastics), thereby mitigating the trade-off between permeability and selectivity commonly encountered in conventional GO membranes.[37,43,44] The slightly higher permeance observed for salt solutions was likely caused by ion-induced adjustments within the FFG nanochannels (such as subtle channel swelling and reduced interfacial friction), which together lowered the hydraulic resistance relative to pure water.[45-47] In addition, due to the clogging of the pore structure in the FFG membrane by pollutants, the permeance of the membranes to nano-plastics (> 2443 L m^{-2} h^{-1} bar^{-1}) and organic dyes (> 1950 L m^{-2} h^{-1} bar^{-1}) was lower than that of pure water.[18]

As the operating pressure increased, the linearly augmented water permeance of the FFG membrane confirmed the formed interconnected channels and thin *S*-channels (Figure S37A). Moreover, the goodness of fit between the water permeance and loading mass of FFG membrane was as high as 0.84 (Figure S37B), demonstrating the superiority and structural stability of these water transport channels. In conclusion, the separation performance of FFG membranes significantly surpassed that of reported membrane materials (Figure 2D and Table S4).[6,48-61] In addition, the FFG membrane was capable of filtering pollutants under hydrostatic pressure even without additional operating pressure (Figures 2E-F, S38 & Video S1), confirming its excellent practicality for sustainable water purification. Remarkably, the FFG membrane maintained stable rejection performance during the 360 min of filtration for

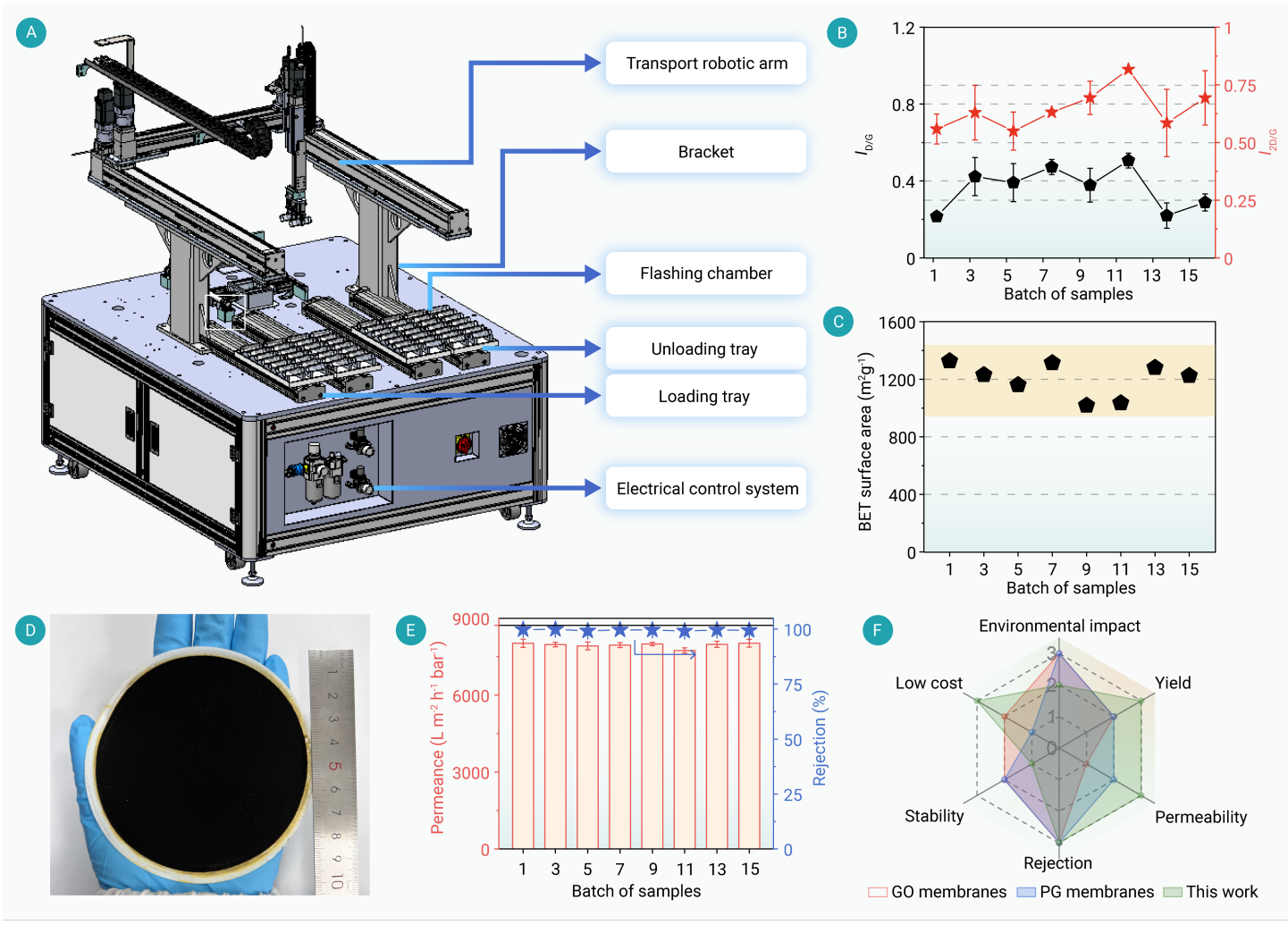


Figure 4. Continuous large-scale synthesis of FFG membranes for water purification (A) Schematic of pilot-scale devices for the continuous production of FG. In this work, two samples were mixed into a batch to facilitate the analysis of the structure and application of FG materials at the pilot-scale. (B) Analysis of Raman spectra showed the D/G and 2D/G intensity ratios (N=3). (C) The BET surface area of each batch of FG materials was measured at the pilot-scale. (D) Digital photos of expanded FFG membranes. (E) Each batch of FFG membranes for $FeCl_3$ separation with a constant concentration of 50 mg L^{-1} at 1 bar. (F) Comparison of properties and performance of different membrane products, including FFG, GO, and porous graphene (PG) membranes. Each product was evaluated in terms of yield, low cost, environmental impact, permeability, rejection, and stability. The numbers 1, 2 and 3 indicated low, medium, and high levels, respectively. Detailed calculations were shown in Table S6.

methyl blue and Fe^{3+} (Figure 2G). However, the FFG membrane exhibited a gradual flux decline during prolonged operation, which can be attributed to the minor fouling effects and concentration polarization (Figure S39).

Moreover, in some remote or underdeveloped areas, where water sources or transportation pipelines may be contaminated with pollutants (such as metal ions and organic matter), portable filters can effectively facilitate the acquisition of purified water without additional operations. For this purpose, a filter cup incorporating an FFG membrane was designed for household drinking water purification (Figure 2H). As demonstrated in Video S2, the filter cup can be installed directly onto a faucet, providing 6 L of clean water per day (8 h) under hydrostatic pressure, thereby meeting the drinking water needs of two individuals. As shown in Figure 2I, nearly 1000 mL of polluted water (containing Fe or perfluorooctanoic acids) was effectively filtered by this device, resulting in clean water. This portable FFG membrane device exhibited effective interception of pollutants, ranging from ions to molecules, highlighting its potential for practical water purification.

FFG membranes with thin *S*-channels for rapid water transport

Certainly, the path length of water molecules transported through the thin *S*-channel, which combined nanopores and interlayer spacing, was shorter than that of the traditional *Z*-channel (Figure 3A & Video S3). To verify the separation mechanism of the FFG membrane with *S*-channels, the trajectories of water molecules and ions or particles through the upper and lower layered stacked nanochannels, including interlayer spacing and nanopores, were verified by molecular dynamics (MD) simulation. As shown in Figures 3B & S40, the simulated defect system consisted of four centrally defective graphene sheets with a pore diameter of approximately 3.0 nm, forming a two-layer stacked graphene membrane. For comparison, a filtration system with perfect graphene sheets was also constructed, as illustrated in Figures S40-S41. Notably, in the perfect system, water molecules only transport along the *Z*-channel, resulting in the water layer thickness on the draw side gradually increasing to about 7 nm at 30 ns (Figure 3C). In the defect system, water molecules can easily penetrate through multiple nanochannels, primarily the *S*-channels, leading to a water layer thickness on the draw side increasing to about 8.5 nm within 30 ns (Figure 3D). Moreover, the actual path length of water molecules in the defect system (thin *S*-channel) was less tortuous than that in the perfect system (*Z*-channel), effectively shortening their transport distance (Figure 3E). Consequently, the number of water molecules permeating each graphene sheet in the defect system was 6.4 times that of the perfect system (Figure 3F), indicating that the FFG membrane with thin *S*-channels exhibited superior water permeance. Due to the narrow interlayer spacing in both systems, Fe^{3+} could not pass through the perfect system within 30 ns, while only two Fe^{3+} ions escaped through the nanopore structure in the defect system (Figure 3G). For larger nano-plastic particles, modeled by carbon nanotubes, the steric hindrance effect prevented their penetration through the layer spacing and nanopores. Therefore, it can be inferred that the addition of a certain degree of defect in the FFG

membrane can optimize the trade-off between permeability and selectivity.

Notably, the pore size between the upper and lower layers of the FFG membrane required further investigation to prevent the direct formation of the *I*-channel, which could lead to solute escape without being rejected by the interlayer spacing (Figure S42). Although the MD result indicated that as the pore size increased, water molecules could easily penetrate the thin *S*-channels (Figures S43-S44). However, when the pore diameter was close to the threshold, solutes (Fe^{3+} and Cl^-) escaped from the *I*-channels, causing the rejection rate to drop sharply to less than 50% (Figure S43C). In conclusion, the FFG membrane simultaneously achieves ultrafast water permeance and complete ion rejection by leveraging pore-enhanced water transport pathways and molecular-sieving mechanism in narrow interlayer channels, effectively overcoming the conventional trade-off between permeability and selectivity.

Potential applications of FFG membranes

We have made some forward-looking efforts in many aspects to improve the practicality of the FFG membrane. Firstly, with the aim of large-scale production, we completed the development of a pilot-scale device to achieve the continuous production of FG precursors (Figures 4A & S45).[29] The FJH reaction was optimized by regulating the discharge voltage and sample loading weight to accommodate the amplification effect between the laboratory and pilot-scale devices. The precursor (PC-1) was subjected to similar Joule heating using laboratory and pilot-scale devices, resulting in a production of approximately 122293 g h^{-1} m^{-2} electrode for FG (9.6 g h^{-1}, Figure S45B & Table S5). Fortunately, this continuous production system proved to be very stable (Figures S46–S48), and the structure of the obtained FG was not significantly different from that produced by previous laboratory-scale devices, as confirmed by Raman, BET, and pore size distribution analyses (Figures 4B–C, S49–S50 & Table S5). Additionally, the practicality and versatility of FFG membrane materials were realized by expanding their application scenarios. In remote areas with outdated infrastructure or wilderness settings, access to purified drinking water is often limited during critical situations. In response, the FFG membrane filtration device was improved to be portable, increasing the effective membrane area by about 75 cm^2 (Figure 4D). Most importantly, this FFG membrane also demonstrated superior water permeance (~ 7948 L m^{-2} h^{-1} bar^{-1}) and excellent rejection (> 99.9%) for $FeCl_3$ (Figure 4E). These results demonstrated the feasibility of large-area FFG membrane integration without significant loss of separation performance.

CONCLUSIONS

In summary, the turbostratically stacked layers of the FFG membrane formed well-developed interconnected channels and numerous thin *S*-channels, significantly shortening water transport pathways and enabling ultrafast water purification. The combined effects of nanopores and interlaminar channels enabled the FFG membrane to achieve high permeability without compromising selectivity, resulting in rapid and efficient removal of molecular and ionic pollutants during filtration. These properties enabled FFG membranes to facilitate water purification without additional pressure, highlighting their potential for sustainable and energy-efficient water treatment. Building on the established technology used for producing graphene from waste biomass, the FFG membrane prepared in this study offers a more cost-effective and environmentally advantageous alternative to conventional membranes made from two-dimensional materials (Figure 4F & Table S6).

Given its excellent separation performance, high water permeance, cost-effective fabrication utilizing waste-derived precursors, as well as low energy consumption and overall cost, the proposed portable device made from FFG membranes shows significant promise for water purification in field and household applications. Given its excellent separation performance, high water permeance, cost-effective fabrication utilizing waste-derived precursors, as well as satisfactory energy consumption and cost, the proposed portable device made from FFG membranes shows promise for water purification in field and household applications. To facilitate the translation of this technology from laboratory-scale development to practical applications, future efforts should focus on scalable membrane manufacturing, long-term stability and fouling resistance in complex real-water matrices, and life-cycle and techno-economic assessments to optimize overall costs.

Therefore, beyond the specific FFG membrane developed in this study, the turbostratic architecture and interconnected transport pathways provide a rational strategy for optimizing membrane structures to simultaneously enhance water transport and contaminant rejection. Crucially, the ability of the FFG membrane to operate efficiently at zero or low applied pressure provides a promising pathway toward low-energy and decentralized water purification, offering broad implications for mitigating global water pollution and addressing water scarcity in resource-limited areas.

REFERENCES

1. Chen C., Chen J., Peng Y., et al. (2024). Multifunctional coatings of graphene oxide: New membranes for proton permeation and salt rejection. *Matter* **7**:1259–1274. DOI:10.1016/j.matt.2024.01.014
2. Chen L., Shi G., Shen J., et al. (2017). Ion sieving in graphene oxide membranes via cationic control of interlayer spacing. *Nature* **550**:380–383. DOI:10.1038/nature24044
3. Kang J., Ko Y., Kim J. P., et al. (2023). Microwave-assisted design of nanoporous graphene membrane for ultrafast and switchable organic solvent nanofiltration. *Nat. Commun.* **14**:901. DOI:10.1038/s41467-023-36524-x
4. Surwade S. P., Smirnov S. N., Vlassiouk I. V., et al. (2015). Water desalination using nanoporous single-layer graphene. *Nat. Nanotechnol.* **10**:459–464. DOI:10.1038/nnano.2015.37
5. Yang Y., Yang X., Liang L., et al. (2019). Large-area graphene-nanomesh/carbon-nanotube hybrid membranes for ionic and molecular nanofiltration. *Science* **364**:1057–1062. DOI:10.1126/science.aau5321
6. Zhang W. H., Yin M. J., Zhao Q., et al. (2021). Graphene oxide membranes with stable porous structure for ultrafast water transport. *Nat. Nanotechnol.* **16**:337–343. DOI:10.1038/s41565-020-00833-9
7. Liu H., Wang H. and Zhang X. (2015). Facile fabrication of freestanding ultrathin reduced graphene oxide membranes for water purification. *Adv. Mater.* **27**:249–254. DOI:10.1002/adma.201404054
8. Joshi R. K., Carbone P., Wang F. C., et al. (2014). Precise and ultrafast molecular sieving through graphene oxide membranes. *Science* **343**:752–754. DOI:10.1126/science.1245711
9. Zhu Z., Song M., Qu F., et al. (2024). Engineering multinanochannel polymer-intercalated graphene oxide membrane for strict volatile sieving in membrane distillation. *Environ. Sci. Technol.* **58**:1399–1409. DOI:10.1021/acs.est.3c08452
10. Dong Y., Lyu Q., Lin L. C., et al. (2024). Ultrastable ceramic-based metal–organic framework membranes with missing linkers for robust desalination. *Nat. Water* **2**:464–474. DOI:10.1038/s44221-024-00218-5
11. Ren Y., Chong B., Xu W., et al. (2022). Coordination-driven structure reconstruction in polymer of intrinsic microporosity membranes for efficient propylene/propane separation. *The Innovation* **3**. DOI:10.1016/j.xinn.2022.100334.
12. Mi B. (2019). Scaling up nanoporous graphene membranes. *Science* **364**:1033–1034. DOI:10.1126/science.aax3103
13. Huang H., Shi H., Das P., et al. (2020). The chemistry and promising applications of graphene and porous graphene materials. *Adv. Funct. Mater.* **30**:1909035. DOI:10.1002/adfm.201909035
14. Zhang Z., Simon A., Abetz C., et al. (2021). Hybrid organic–inorganic–organic isoporous membranes with tunable pore sizes and functionalities for molecular separation. *Adv. Mater.* **33**:2105251. DOI:10.1002/adma.202105251
15. Warkiani M. E., Bhagat A. A. S., Khoo B. L., et al. (2013). Isoporous micro/nanoengineered membranes. *ACS Nano* **7**:1882–1904. DOI:10.1021/nn305616k
16. Fane A. G., Wang R. and Hu M. X. (2015). Synthetic membranes for water purification: Status and future. *Angew. Chem. Int. Ed.* **54**:3368–3386. DOI:10.1002/anie.201409783
17. Lin Y., Liao Y., Chen Z., et al. (2017). Holey graphene: A unique structural derivative of graphene. *Mater. Res. Lett.* **5**:209–234. DOI:10.1080/21663831.2016.1271047
18. Kang J., Choi Y., Kim J. H., et al. (2021). Functionalized nanoporous graphene membrane with ultrafast and stable nanofiltration. *J. Membr. Sci.* **618**:118635. DOI:10.1016/j.memsci.2020.118635
19. Yuan B., Wang M., Wang B., et al. (2020). Cross-linked graphene oxide framework membranes with robust nano-channels for enhanced sieving ability. *Environ. Sci. Technol.* **54**:15442–15453. DOI:10.1021/acs.est.0c05387
20. Seo D. H., Pineda S., Woo Y. C., et al. (2018). Anti-fouling graphene-based membranes for effective water desalination. *Nat. Commun.* **9**:683. DOI:10.1038/s41467-018-02871-3
21. Sun M. and Li J. (2018). Graphene oxide membranes: Functional structures, preparation and environmental applications. *Nano Today* **20**:121–137. DOI:10.1016/j.nantod.2018.04.007
22. Cheng C., Jiang G., Garvey C. J., et al. (2016). Ion transport in complex layered graphene-based membranes with tuneable interlayer spacing. *Sci. Adv.* **2**:e1501272. DOI:10.1126/sciadv.1501272
23. Gao F., Chen W., Eatman J. G., et al. (2024). Pushing the limits of size selectivity in nanoscale solute separations. *Nat. Water* **2**:521–530. DOI:10.1038/s44221-024-

00252-3
24. Liu G., Jin W. and Xu N. (2015). Graphene-based membranes. *Chem. Soc. Rev.* **44**:5016–5030. DOI:10.1039/C4CS00423J
25. Yang L., Xiao X., Shen S., et al. (2022). Recent advances in graphene oxide membranes for nanofiltration. *ACS Appl. Nano Mater.* **5**:3121–3145. DOI:10.1021/acsanm.1c04469
26. Huang J., Zhang Y., Guo J., et al. (2024). Polymeric membranes with highly homogenized nanopores for ultrafast water purification. *Nat. Sustain.* **7**:901–909. DOI:10.1038/s41893-024-01371-1
27. Luong D. X., Bets K. V., Algozeeb W. A., et al. (2020). Gram-scale bottom-up flash graphene synthesis. *Nature* **577**:647–651. DOI:10.1038/s41586-020-1938-0
28. Jia C., Pang M., Lu Y., et al. (2022). Graphene environmental footprint greatly reduced when derived from biomass waste via flash Joule heating. *One Earth* **5**:1394–1403. DOI:10.1016/j.oneear.2022.11.006
29. Zhu X., Lin L., Pang M., et al. (2024). Continuous and low-carbon production of biomass flash graphene. *Nat. Commun.* **15**:3218. DOI:10.1038/s41467-024-47603-y
30. Phillips J. C., Braun R., Wang W., et al. (2005). Scalable molecular dynamics with NAMD. *J. Comput. Chem.* **26**:1781–1802. DOI:10.1002/jcc.20289
31. Geng H., Liu X., Shi G., et al. (2017). Graphene oxide restricts growth and recrystallization of ice crystals. *Angew. Chem. Int. Ed.* **56**:997–1001. DOI:10.1002/anie.201609230
32. Liu X., Geng H., Sheng N., et al. (2020). Suppressing ice growth by integrating the dual characteristics of antifreeze proteins into biomimetic two-dimensional graphene derivatives. *J. Mater. Chem. A* **8**:23555–23562. DOI:10.1039/D0TA06421A
33. Tu Y., Lv M., Xiu P., et al. (2013). Destructive extraction of phospholipids from Escherichia coli membranes by graphene nanosheets. *Nat. Nanotechnol.* **8**:594–601. DOI:10.1038/nnano.2013.125
34. Jorgensen W. L., Chandrasekhar J., Madura J. D., et al. (1983). Comparison of simple potential functions for simulating liquid water. *J. Chem. Phys.* **79**:926–935. DOI:10.1063/1.445869
35. MacKerell A. D., Jr., Bashford D., Bellott M., et al. (1998). All-atom empirical potential for molecular modeling and dynamics studies of proteins. *J. Phys. Chem. B* **102**:3586–3616. DOI:10.1021/jp973084f
36. Essmann U., Perera L., Berkowitz M. L., et al. (1995). A smooth particle mesh Ewald method. *J. Chem. Phys.* **103**:8577–8593. DOI:10.1063/1.470117
37. Yan L., Chen J., Zhang Z., et al. (2025). Reduced graphene oxide membrane with small nanosheets for efficient and ultrafast removal of both microplastics and small molecules. *J. Hazard. Mater.* **487**:137078. DOI:10.1016/j.jhazmat.2024.137078
38. Aba N. D., Chong J. Y., Wang B., et al. (2015). Graphene oxide membranes on ceramic hollow fibers – microstructural stability and nanofiltration performance. *J. Membr. Sci.* **484**:87–94. DOI:10.1016/j.memsci.2015.03.001
39. Kang Y., Hu T., Wang Y., et al. (2023). Nanoconfinement enabled non-covalently decorated MXene membranes for ion-sieving. *Nat. Commun.* **14**:4075. DOI:10.1038/s41467-023-39533-y
40. Wu T., Wang Z., Lu Y., et al. (2021). Graphene oxide membranes for tunable ion sieving in acidic radioactive waste. *Adv. Sci.* **8**:2002717. DOI:10.1002/advs.202002717
41. Mahmoud K. A., Mansoor B., Mansour A., et al. (2015). Functional graphene nanosheets: The next generation membranes for water desalination. *Desalination* **356**:208–225. DOI:10.1016/j.desal.2014.10.022
42. Mi B. (2014). Graphene oxide membranes for ionic and molecular sieving. *Science* **343**:740–742. DOI:10.1126/science.1250247
43. Jian L., Qiu Y., Zhang Z., et al. (2025). Reduced graphene oxide membrane with wrinkled surfaces for ultrafast and stable microplastics removal. *J. Environ. Chem. Eng.* **13**:120454. DOI:10.1016/j.jece.2025.120454
44. Sun J., Xiong Y., Jia H., et al. (2024). Superb microplastics separation performance of graphene oxide tuned by laser bombardment. *J. Hazard. Mater.* **461**:132599. DOI:10.1016/j.jhazmat.2023.132599
45. Cohen-Tanugi D. and Grossman J. C. (2015). Nanoporous graphene as a reverse osmosis membrane: Recent insights from theory and simulation. *Desalination* **366**:59–70. DOI:10.1016/j.desal.2014.12.046
46. Zhang M., Guan K., Ji Y., et al. (2019). Controllable ion transport by surface-charged graphene oxide membrane. *Nat. Commun.* **10**:1253. DOI:10.1038/s41467-019-09286-8
47. Yang T., Lin H., Loh K. P., et al. (2019). Fundamental transport mechanisms and advancements of graphene oxide membranes for molecular separation. *Chem. Mater.* **31**:1829–1846. DOI:10.1021/acs.chemmater.8b03820
48. Yang R., Fan Y., Yu R., et al. (2021). Robust reduced graphene oxide membranes with high water permeance enhanced by K^+ modification. *J. Membr. Sci.* **635**:119437. DOI:10.1016/j.memsci.2021.119437
49. Liu J., Wang S., Yang R., et al. (2022). Bio-inspired graphene oxide-amino acid cross-linked framework membrane trigger high water permeance and high metal ions rejection. *J. Membr. Sci.* **659**:120745. DOI:10.1016/j.memsci.2022.120745
50. Dai F., Zhou F., Chen J., et al. (2021). Ultrahigh water permeation with a high multivalent metal ion rejection rate through graphene oxide membranes. *J. Mater. Chem. A* **9**:10672–10677. DOI:10.1039/D1TA00647A
51. Wang Z., Wei Y. M., Xu Z. L., et al. (2016). Preparation, characterization and solvent resistance of γ-Al_2O_3/α-Al_2O_3 inorganic hollow fiber nanofiltration membrane. *J. Membr. Sci.* **503**:69–80. DOI:10.1016/j.memsci.2015.12.039
52. Yi R., Xia X., Yang R., et al. (2021). Selective reduction of epoxy groups in graphene oxide membrane for ultrahigh water permeation. *Carbon* **172**:228–235. DOI:10.1016/j.carbon.2020.09.076
53. Yang Q., Su Y., Chi C., et al. (2017). Ultrathin graphene-based membrane with precise molecular sieving and ultrafast solvent permeation. *Nat. Mater.* **16**:1198–1202. DOI:10.1038/nmat5025
54. Liu T., Zhang Y., Shan Z., et al. (2023). Covalent organic framework membrane for efficient removal of emerging trace organic contaminants from water. *Nat. Water* **1**:1059–1067. DOI:10.1038/s44221-023-00162-w
55. Zhang W., Xu H., Xie F., et al. (2022). General synthesis of ultrafine metal oxide/reduced graphene oxide nanocomposites for ultrahigh-flux nanofiltration membrane. *Nat. Commun.* **13**:471. DOI:10.1038/s41467-022-28180-4
56. Akbari A., Sheath P., Martin S. T., et al. (2016). Large-area graphene-based nanofiltration membranes by shear alignment of discotic nematic liquid crystals of graphene oxide. *Nat. Commun.* **7**:10891. DOI:10.1038/ncomms10891
57. Liu W., Li Y., Xu L., et al. (2022). Biomimic heterostructured graphene oxide membranes via supramolecular-mediated intercalation assembly for efficient water transport. *Small* **18**:2200461. DOI:10.1002/smll.202200461
58. Han C., Jiang J., Mu L., et al. (2025). Quasi-vertically asymmetric channels of graphene oxide membrane for ultrafast ion sieving. *Nat. Commun.* **16**:1020. DOI:10.1038/s41467-025-56358-z
59. Dai F., Gu Z., Hu S., et al. (2024). Unexpected self-assembly of nanographene oxide membranes upon electron beam irradiation for ultrafast ion sieving. *Adv. Sci.* **11**:2404001. DOI:10.1002/advs.202404001
60. Liu H., Mu M., Graham N. J. D., et al. (2024). Alkaline-oxidized MXene composite membrane of ultra high flux and advanced rejection performance for water purification. *J. Membr. Sci.* **698**:122604. DOI:10.1016/j.memsci.2024.122604
61. Li Y., Luo H., Ji W., et al. (2023). Visible-light-driven photocatalytic ZnO@Ti3C2Tx MXene nanofiltration membranes for enhanced organic dyes removal. *Sep. Purif. Technol.* **323**:124420. DOI:10.1016/j.seppur.2023.124420

FUNDING AND ACKNOWLEDGMENTS

This work was supported by the National Natural Science Foundation of China (No. 42225701 to Y.W., No. 22276040 to X.Z.). The funders had no role in study design, data collection and analysis, decision to publish, or preparation of the manuscript.

AUTHOR CONTRIBUTIONS

X.Z. and G.S. conceived the initial idea and experimental design. C.J., J.C., and L.Y. performed the experiments and characterizations with the assistance of L.S., F.Y., and J.L., X.Z., G.S., and Y.L. supervised the experiment. X.L., G.S., X. Z., and B. X. performed molecular dynamics simulations and analyzed the data. C.J. and J.W. performed the STEM experiments and analyzed the data. All authors contributed to the analysis and discussion of the data. C.J. wrote the original draft of the manuscript. X.Z., G.S., Y. W., Y.L., S.Z., S.L., M.W., J. Z., and F. W. reviewed and edited the manuscript. All authors contributed to and approved the manuscript.

DECLARATION OF INTERESTS

The authors declare no competing interests.

DATA AND CODE AVAILABILITY

Data are available from the corresponding author upon reasonable request.

SUPPLEMENTAL INFORMATION

It can be found online at https://doi.org/10.59717/j.xinn-mater.2026.100224.